

## Article

# Leaf Water Potential in a Mixed Mediterranean Forest from Machine Learning and Unmanned Aerial Vehicle (UAV)-Based Hyperspectral Imaging

Netanel Fishman <sup>1</sup>, Yehuda Yungstein <sup>1,2</sup>, Assaf Yaakobi <sup>3</sup>, Sophie Obersteiner <sup>3</sup>, Laura Rez <sup>3</sup>, Gabriel Mulero <sup>1,2</sup>, Yaron Michael <sup>1</sup>, Tamir Klein <sup>3</sup> and David Helman <sup>1,2,\*</sup>

<sup>1</sup> Department of Soil and Water Sciences, Institute of Environmental Sciences, The Robert H. Smith Faculty of Agriculture, Food and Environment, The Hebrew University of Jerusalem, Rehovot 7610001, Israel; netanel.fishman@mail.huji.ac.il (N.F.); yehuda.yungstein@mail.huji.ac.il (Y.Y.); gabriel.mulero@mail.huji.ac.il (G.M.); yaron.michael@mail.huji.ac.il (Y.M.)

<sup>2</sup> The Advanced School for Environmental Studies, The Hebrew University of Jerusalem, Givat Ram, Jerusalem 9190401, Israel

<sup>3</sup> Department of Plant and Environmental Sciences, Weizmann Institute of Science, Rehovot 7610001, Israel; assaf.yaakobi@weizmann.ac.il (A.Y.); sophie.obersteiner@weizmann.ac.il (S.O.); laura.rez@weizmann.ac.il (L.R.); tamir.klein@weizmann.ac.il (T.K.)

\* Correspondence: david.helman@mail.huji.ac.il

**Abstract:** Leaf water potential ( $\psi_{leaf}$ ) is a key indicator of plant water status, but its measurement is labor-intensive and limited in spatial coverage. While remote sensing has emerged as a useful tool for estimating vegetation water status,  $\psi_{leaf}$  remains unexplored, particularly in mixed forests. Here, we use spectral indices derived from unmanned aerial vehicle-based hyperspectral imaging and machine learning algorithms to assess  $\psi_{leaf}$  in a mixed, multi-species Mediterranean forest comprised of five key woody species: *Pinus halepensis*, *Quercus calliprinos*, *Cupressus sempervirens*, *Ceratonia siliqua*, and *Pistacia lentiscus*. Hyperspectral images (400–1000 nm) were acquired monthly over one year, concurrent with  $\psi_{leaf}$  measurements in each species. Twelve spectral indices and thousands of normalized difference spectral index (NDSI) combinations were evaluated. Three machine learning algorithms—random forest (RF), extreme gradient boosting (XGBoost), and support vector machine (SVM)—were used to model  $\psi_{leaf}$ . We compared the machine learning model results with linear models based on spectral indices and the NDSI. SVM, using species information as a feature, performed the best with a relatively good  $\psi_{leaf}$  assessment ( $R^2 = 0.53$ ; RMSE = 0.67 MPa; rRMSE = 28%), especially considering the small seasonal variance in  $\psi_{leaf}$  ( $\pm\sigma = 0.8$  MPa). Predictions were best for *Cupressus sempervirens* ( $R^2 = 0.80$ ) and *Pistacia lentiscus* ( $R^2 = 0.49$ ), which had the largest  $\psi_{leaf}$  variances ( $\pm\sigma > 1$  MPa). Aggregating data at the plot scale in a ‘general’ model markedly improved the  $\psi_{leaf}$  model ( $R^2 = 0.79$ , RMSE = 0.31 MPa; rRMSE = 13%), providing a promising tool for monitoring mixed forest  $\psi_{leaf}$ . The fact that a non-species-specific, ‘general’ model could predict  $\psi_{leaf}$  implies that such a model can also be used with coarser resolution satellite data. Our study demonstrates the potential of combining hyperspectral imagery with machine learning for non-invasive  $\psi_{leaf}$  estimation in mixed forests while highlighting challenges in capturing interspecies variability.



Academic Editor: Junjun Jiang

Received: 21 November 2024

Revised: 22 December 2024

Accepted: 25 December 2024

Published: 31 December 2024

**Citation:** Fishman, N.; Yungstein, Y.; Yaakobi, A.; Obersteiner, S.; Rez, L.; Mulero, G.; Michael, Y.; Klein, T.; Helman, D. Leaf Water Potential in a Mixed Mediterranean Forest from Machine Learning and Unmanned Aerial Vehicle (UAV)-Based Hyperspectral Imaging. *Remote Sens.* **2025**, *17*, 106. <https://doi.org/10.3390/rs17010106>

**Copyright:** © 2024 by the authors.

Licensee MDPI, Basel, Switzerland.

This article is an open access article distributed under the terms and conditions of the Creative Commons Attribution (CC BY) license

(<https://creativecommons.org/licenses/by/4.0/>).

**Keywords:** NDVI; random forest; remote sensing; SVM; water; XGBoost

## 1. Introduction

Forests increasingly face harsh conditions, leading to worldwide tree mortality in the last few decades [1]. This trend is expected to aggravate under projected climate change. Rising temperatures and altered precipitation patterns will induce severe drought conditions in many regions [2]. Despite their adaptation capacity, many forest species might not cope with such conditions, leading to a decline in growth rates and increased mortality [3,4]. Monitoring forests' water status is vital to facing such expanded adverse effects. This requires developing accurate, efficient, and large-scale assessment methods [5].

One of the most valuable metrics for characterizing drought stress and water status in woody species is the leaf water potential ( $\psi_{leaf}$ ).  $\psi_{leaf}$  represents the degree of stability of the water in the xylem transport conduits of the trees by becoming more negative as the drought stress increases [6].  $\psi_{leaf}$  is a key indicator of plant water status and can provide valuable insights into the severity of drought stress experienced by the tree [7]. However, measuring  $\psi_{leaf}$  in the field is a time-consuming and labor-intensive process, typically involving the use of pressure chambers on individual leaves [8]. This approach limits the spatial coverage and temporal resolution of  $\psi_{leaf}$  measurements, making it challenging to capture the heterogeneity of drought stress within and across forest stands.

Remote sensing offers a promising solution to this challenge, enabling the rapid and non-invasive assessment of vegetation status across large areas [9,10]. Hyperspectral reflectance information obtained from satellites or drone-based sensors has been widely used to estimate various plant traits, including the leaf area index, chlorophyll content, water content, transpiration rate, and water use efficiency [11–19]. The physical basis for using spectral information to estimate plant traits is based on the interaction of light with plants' biophysical and biochemical characteristics. Plant traits corresponding to water content or stress can directly influence absorption in the NIR region, particularly around the 970 nm and 1200 nm water absorption bands, as well as in the SWIR, particularly 1450, 1900, and 1950 nm [20]. Other indirect responses of water-related stress that may lead to variations in pigment concentrations within the plant's intercellular organelles primarily affect reflectance in the visible range [21].

Thus, several studies have explored the potential for using spectral vegetation indices, a mathematical combination of two or more bands derived from remote sensing data, to assess  $\psi_{leaf}$  across vegetation types. Raj et al. [22] detailed several water absorption bands in the visible and NIR regions useful for monitoring water-related variables like  $\psi_{leaf}$ . They identified seven bands in the 400–1000 nm, which are sensitive to vibrational overtone frequencies of O-H bonds of water molecules, and created four normalized indices that showed a high correlation to the leaf water content of Maize crops. Peñuelas et al. [23] developed the water band index based on near-infrared (NIR) reflectance ( $R_{970}/R_{900}$ ) to estimate  $\psi_{leaf}$  under salinity stress conditions. Stimson et al. [24] demonstrated that drought stress in two tree species (*Pinus edulis* and *Juniperus monosperma*) could be quantified using indices incorporating 980 nm and 1200 nm wavelength bands, significantly correlated with the measured  $\psi_{leaf}$ . Italiano et al. [25] showed corresponding temporal patterns that had a positive linear relationship with earlywood hydraulic diameter (linked to water conductivity) in drought-prone Mediterranean forests using common vegetation indices such as the NDVI, EVI, and NDWI.

Additionally, Othman et al. [26], analyzing Landsat satellite imagery, found that the shortwave-infrared (SWIR) band ratio effectively predicted  $\psi_{leaf}$  in pecan orchards. More recently, using three SWIR bands, Wang et al. [27] proposed a modified vegetation index ( $(R_{1740}-R_{2370})/(R_{1740}-R_{1750})$ ), which showed a strong correlation with  $\psi_{leaf}$  across different leaf structures. Such a myriad of studies, among others, suggest that remotely sensed spectral data could be successfully used for monitoring  $\psi_{leaf}$  in complex systems such as

mixed forests. Yet, such complex systems may require models that account for nonlinear relationships between the remotely sensed data and  $\psi_{leaf}$ .

Machine learning techniques have shown great promise for modeling plant water content and status using remote sensing data. Machine learning algorithms can effectively capture the complex and nonlinear relationships between spectral reflectance patterns and plant physiological traits (e.g., Li et al. [28]). Several studies have successfully applied machine learning algorithms such as random forests (RFs), support vector machine (SVM), and artificial neural networks (ANNs) to predict leaf water content, relative water content, and equivalent water thickness from hyperspectral and multispectral imagery [29–31].

Despite the progress made in applying remote sensing to assess  $\psi_{leaf}$ , there remains a gap in our understanding of how these techniques perform in diverse, mixed-species forests at high spatial resolutions (<1 m). To the best of our knowledge, no study has combined high-spatial-resolution remote sensing data acquired from sensors onboard unmanned aerial vehicles (UAVs) with machine learning algorithms to predict  $\psi_{leaf}$  in mixed forest stands. Many Mediterranean forests, for example, are characterized by a complex mosaic of woody species with varying drought tolerances and water use strategies [32,33]. To accurately assess the water status of these forests, it is necessary to develop remote sensing methods that can account for such heterogeneity and species-specific  $\psi_{leaf}$  at fine spatial scales [34]. Then, generated  $\psi_{leaf}$  maps could be used to point at specific stands or stand areas under stress conditions, allowing for precursory intervention. This is particularly important in places like Israel, where about half of the forested areas are planted and managed by the Jewish National Fund (JNF [35]). Such monitoring can help detect stands under stress and treat the stands with irrigation or thinning the stand density under pressure [36,37].

Here, we address the above research gap by examining the use of high-spatial-resolution UAV-derived hyperspectral imagery taken over a year in open-field experimental plots to assess  $\psi_{leaf}$  in five key Mediterranean woody species. We developed machine learning models based on the hyperspectral data and field  $\psi_{leaf}$  measurements and compared the models with commonly used spectral indices to assess  $\psi_{leaf}$ . We evaluated the ability of spectral reflectance data and machine learning models to capture plot and species-specific  $\psi_{leaf}$  changes. We hypothesize that (i)  $\psi_{leaf}$  would be easier to model for species with a broader range of  $\psi_{leaf}$  values than species displaying a narrow range of values. We also hypothesize that (ii) machine learning algorithms should significantly enhance the ability to predict  $\psi_{leaf}$  compared to simple linear regression models using spectral indices, particularly those based on nonlinear relationships.

## 2. Data and Methods

### 2.1. Study Site and Experimental Design

The experiment was conducted in Yishi Forest, a semi-arid mixed Mediterranean forest in the Judean foothills, Israel [34,38]. The forest is located 4 km southwest of Beit Shemesh, Israel ( $31^{\circ}43'N$   $34^{\circ}57'E$ , Figure 1). It covers an area of ~650 ha with an average elevation of 300 m a.s.l. and a mean annual precipitation of  $460\text{ mm yr}^{-1}$  (annual mean of the last 20 years). Precipitation occurs mainly from November to May. The mean annual temperature is  $20.4 \pm 6.8\text{ }^{\circ}\text{C}$ , with mean winter (January–March) and summer (June–August) temperatures of  $16.5 \pm 1.9\text{ }^{\circ}\text{C}$  and  $24.1 \pm 7.9\text{ }^{\circ}\text{C}$ , respectively [39]. The predominant soil type in Yishi is terra rossa, which consists of A and C soil horizons, with C horizon soil penetrating the cracks between the weathered limestone bedrock. Soil depth (A horizon) is ~21 cm, ranging from 16 to 25 cm [33].

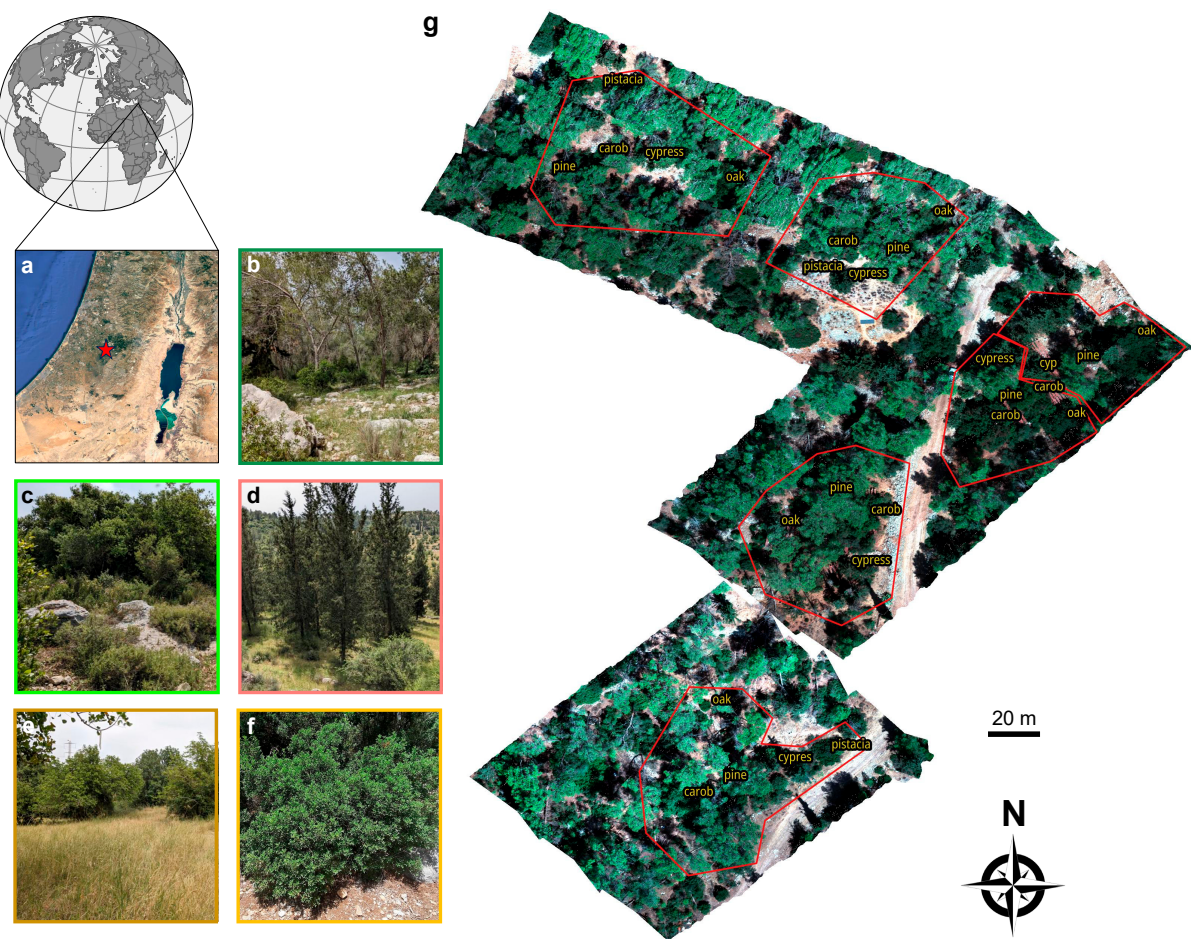


**Figure 1.** (a) The study area (marked by a red star) and the five key Mediterranean woody species comprising Yishi Forest, which includes (b) Pine (*Pinus halepensis*), (c) Oak (*Quercus calliprinos*), (d) Cypress (*Cupressus sempervirens*), (e) Carob (*Ceratonia siliqua*), and (f) Pistacia (*Pistacia lentiscus*). (g) An RGB image derived from the hyperspectral camera onboard an M600 Pro UAV showing the six plots in the studied area.

The vegetation in Yishi is dominated by the planted gymnosperm woody species *Pinus halepensis* (Figure 1b) and *Cupressus sempervirens* (Figure 1d), as well as the local Mediterranean angiosperm woody species *Quercus calliprinos* (Figure 1c), *Ceratonia siliqua* (Figure 1e), and *Pistacia lentiscus* (Figure 1f). In what follows, we will refer to these key woody species by their common English names: Pine, Cypress, Oak, Carob, and Pistacia. These woody species were formerly studied in situ regarding their water relations and carbon management ([33,38], respectively). The forest understory supports a variety of annual plants that thrive from winter to spring.

Six plots, each ~0.05 ha in area, were established within the forest, comprising the five co-occurring woody species (Figure 1g). The plots were divided into two treatments, three plots subjected to rainfall reduction to simulate drought conditions and three control plots under normal rainfall conditions. The rainfall reduction treatment involved installing an open-pipe harvesting system to divert approximately 50% of incident precipitation from the treated plots. Nevertheless, considering the drought-adapted woody species studied here, treatment effects were not expected within the first few years, as reported for a nearby site [40]. Therefore, treatments were not considered in the analysis of this study, but rather, data from both treatments were used together to broaden the range in  $\psi_{leaf}$  to enable more robust modeling.

## 2.2. Field Measurements

$\psi_{leaf}$  was measured using the pressure chamber technique [41]. This method involves enclosing a leaf petiole in a sealed chamber and gradually increasing the pressure inside the chamber until the sap is observed emerging from the cut surface of the petiole. The pressure at which this occurs is equal to the negative of the leaf water potential, providing a direct measurement of the water status within the leaf [42]. Measurements were conducted monthly between October 2021 and March 2023 from 11:00 AM to 1:00 PM to capture maximum daily  $\psi_{leaf}$  values across the season.  $\psi_{leaf}$  was measured once per date in all the 30 trees used in this study (five species in six plots). In a preliminary trial, we measured five leaves per individual tree on a subset of the studied trees. Variations in  $\psi_{leaf}$  among leaves sampled from the same tree were in the magnitude of 2–7%. A major consideration of the field measurements was to complete all measurements within the shortest time possible to avoid significant diurnal variations among the samples. This is paramount when comparing individuals and species in a single day. Thus, to complete the measurements of all 30 trees within 60–90 min (representing similar temperature, humidity, and radiation conditions), having a single pressure chamber instrument and two workers, and following the small  $\psi_{leaf}$  variability observed in our trial, we opted to sample a single leaf per tree (per date). Excised leaves were immediately placed in airtight plastic bags and kept cool to minimize measurement errors from time lags. A total of 30 leaves were sampled per date and measured using a PMS1515 pressure chamber (PMS, Albany, OR, USA). The total number of sampled leaves during the study period was 480 (16 months, 30 leaves per date).

## 2.3. UAV Platform and Spectral Data Acquisition

Hyperspectral imagery was acquired monthly concurrent with the  $\psi_{leaf}$  measurements starting from March 2022 to February 2023, using a Nano-Hyperspec camera (Headwall Photonics, Boston, MA, USA) mounted on a DJI Matrice 600 Pro (M600) Hexacopter. The NanoSpec sensor is a push-broom hyperspectral nano-sensor with 274 spectral bands and 640 spatial pixels within the visible-near-infrared range from 400 nm to 1000 nm. The M600 is controlled via a handheld remote control transmitter and a ground control station with a navigation data link, which sends waypoint navigation information to the aircraft from a laptop computer. The M600 carries a Global Navigation Satellite System (GNSS) and an Inertial Measurement Unit (IMU) (SBG Systems North America, Inc., Chicago, IL, USA).

The images were collected between 11:00 AM and 1:00 PM, concurrent with the  $\psi_{leaf}$  measurements, at the height of 60 m above ground level, providing a spatial resolution of 2–3 cm per pixel. Three flights were required to cover the study area. For radiometric calibration, a 3 m by 3 m in situ gray-white reflectance calibration with three strips and distinct reflectance factors (56%, 30%, and 11% reflectance) was set up within the flight scene in each campaign (date). For geometric corrections, a ground-based GNSS receiver—Trimble SPS585 precision RTK (Trimble Inc., Westminster, CO, USA)—was used to collect static geolocation data to calculate the post-processing kinematic (PPK) flight trajectory using a smoothed best-estimated trajectory (SBET) file generated from the POSpac UAV™ Version 8.9 software tool (Applanix, Richmond Hill, ON, Canada).

## 2.4. Spectral Data Processing

Radiometric calibration, geometric corrections, and ortho-mosaicing were applied to the raw hyperspectral image cubes via the SpectralView software version 3.1.4 (Headwall Photonics, Fitchburg, MA, USA). Shades and non-vegetated areas within the image (Figure 2a) were masked using the Quantum Geographic Information System (QGIS version 3.32.3, Free Software Foundation, Boston, MA, USA). First, the normalized difference vegetation index (NDVI) was calculated, and pixels with NDVI < 0.3 were excluded to

eliminate soil and understory vegetation (Figure 2b). Then, we used near-infrared (NIR) reflectance values below a threshold of 0.07–0.2 to eliminate shaded parts in the canopy since these affect the spectral signal despite changes in  $\psi_{leaf}$ . We found these thresholds suitable for that purpose following trial and error after visually inspecting the clipped RGB (Figure 2c).

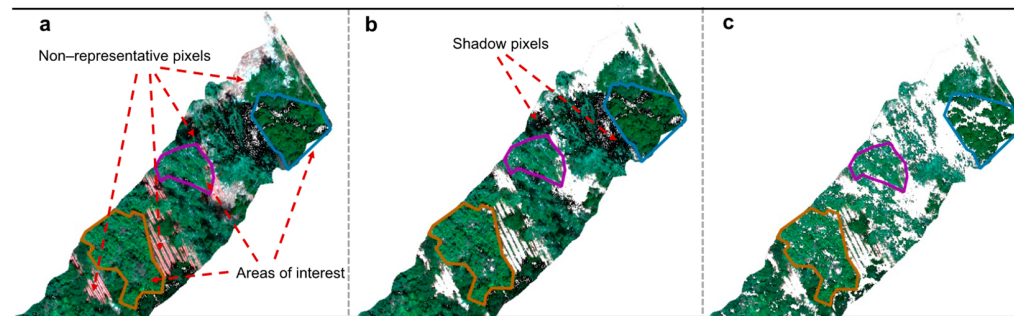


**Figure 2.** An example of masking non-representative pixels within the pre-processing pipeline. (a) The original image with polygons of the areas of interest (i.e., the targeted trees) and non-vegetated pixels within the image. (b) The image after masking non-representative pixels using an NDVI threshold of  $<0.3$  and (c) shaded pixels with an NIR reflectance threshold.

The reflectance values of retained pixels were averaged for each tree canopy, which was manually delineated, to obtain a single mean reflectance spectrum representing the entire canopy. The Savitzky–Golay filter [43], with a window size of 20 bands and second-order polynomials, was applied to eliminate potential artifacts and anomalies in the spectral signatures caused by measurement errors (Figure 3).

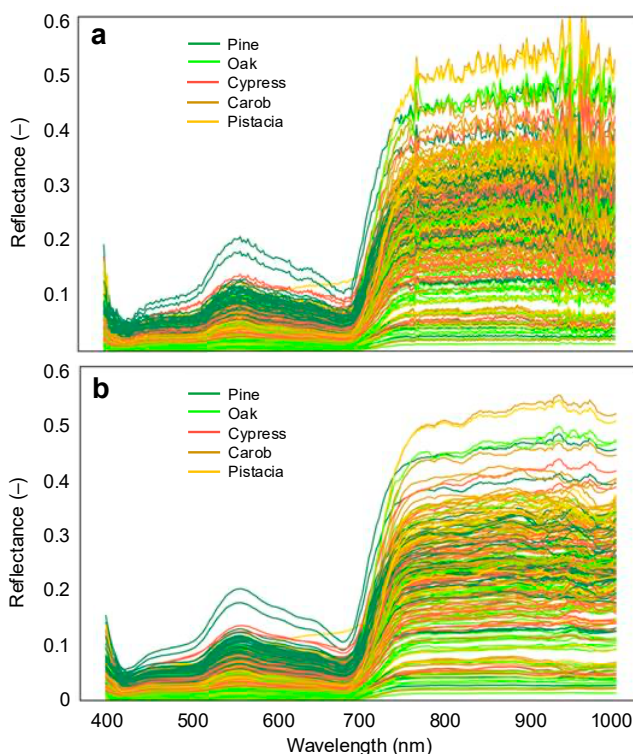


**Figure 3.** Spectral signatures in the 400–1000 nm range (a) before and (b) after applying the Savitzky–Golay filter smoothing. Each line in the graph corresponds to the averaged signature over all pixels in the canopy per each species and date.

After the spectral data processing, the final dataset used within the modeling pipeline resulted in a sample size of  $N = 246$ . The data were randomly split into a 70% training set and a 30% test set for model training and evaluation purposes. This ratio is considered useable and generic within an ML pipeline, especially if one wants a larger data sample to evaluate the model and ensure a more robust transferability to other locations and cases.

### 3. Predictive Models

We followed two approaches to predict  $\psi_{\text{leaves}}$  from the hyperspectral data. First, we used a simple regression approach, whereas the predictor is a spectral index, whether derived in previous studies or generated in this study for all species together as well as for individual species (see Section 3.1). For the same datasets, we also tested the best NDSI, adding one index at a time within a multivariable linear regression (MLR) model. Second, we used the best NDSIs generated from the hyperspectral data in three machine learning algorithms (Section 3.2).

#### 3.1. Spectral Indices

Twelve known spectral indices within the 400–1000 nm range were tested by conducting a simple linear regression with  $\psi_{\text{leaf}}$ . The selected indices were based on their ability to directly and indirectly predict water-related plant traits [44–47]. The normalized difference vegetation index (NDVI), the photochemical reflectance index (PRI), and the enhanced vegetation index version two (EVI2) were tested for their ample use in monitoring vegetation status and dynamics, which showed to be indirectly related to water stress through biophysical changes [44,48,49]. COSBNDI, FOSBNDI, SAPSBNDI, and WASCOSBNDI, which were developed based on seven identified bands sensitive to the vibrational overtone frequencies of O-H bonds of water molecules, were tested due to their strong link to leaf water content [22]. We also used the normalized difference water stress index (NDWSI) and the normalized difference water index (NDWI) because they have been shown to be sensitive to plant water status via canopy structural changes [44,50]. There are several versions of the NDWI [19,51,52]. Here, we used the one based on the 540 and 803 nm bands (Table 1), which incorporates the responses from the visible region of the spectrum (the green band) with canopy structural changes within the NIR region to water-related responses since our hyperspectral data were restricted to the VIS–NIR wavelength range (400–1000 nm). Finally, the water index (WI), developed specifically to assess  $\psi_{\text{leaf}}$ , was tested. The WI gives information about canopy water status with a change in the 970 nm relative to the 900 nm as the water status changes in the leaves [23]. Table 1 summarizes the 12 spectral indices, providing their mathematical formulation.

**Table 1.** Previously published spectral indices used in this study to assess  $\psi_{\text{leaf}}$ .

Index	Name	Formula	Reference
NDVI	Normalized difference vegetation index	$\frac{\rho_{\text{NIR}} - \rho_R}{\rho_{\text{NIR}} + \rho_R}$	[53]
PRI	Photochemical reflectance index	$\frac{\rho_{531} - \rho_{570}}{\rho_{531} + \rho_{570}}$	[54]
940/960	Reflectance ratio of 940 and 960 nm	$\frac{\rho_{940}}{\rho_{960}}$	[55]
940/960/NDVI	Reflectance ratio of 940/960 nm and NDVI	$\frac{\rho_{940} / \rho_{960}}{\text{NDVI}}$	[55]
EVI2	Enhanced vegetation index 2nd version	$2.5 \left( \frac{\rho_{\text{NIR}} - \rho_R}{\rho_{\text{NIR}} + (6 \rho_R) - (7.5 \rho_B) + 1} \right)$	[56]

**Table 1.** Cont.

Index	Name	Formula	Reference
COSBNDI	Combined overtone of stretching bands—normalized difference index	$\frac{\rho_{660} - \rho_{420}}{\rho_{660} + \rho_{420}}$	[22]
FOSBNDI	Forth overtone of stretching bands—normalized difference index	$\frac{\rho_{529} - \rho_{698}}{\rho_{529} + \rho_{698}}$	[22]
SAPSBNDI	Small absorption peak of stretching bands—normalized difference index	$\frac{\rho_{750} - \rho_{970}}{\rho_{750} + \rho_{970}}$	[22]
WASCOSBNDI	Water absorption shoulder due to the combined overtone of stretching bands—normalized difference index	$\frac{\rho_{800} - \rho_{847}}{\rho_{800} + \rho_{847}}$	[22]
NDWSI	Normalized different water stress index	$\frac{\rho_{850} - \rho_{970}}{\rho_{850} + \rho_{970}}$	[50]
NDWI	Normalized different water index	$\frac{\rho_G - \rho_{\text{NIR}}}{\rho_G + \rho_{\text{NIR}}}$	[44]
WI	Water index	$\frac{\rho_{970}}{\rho_{900}}$	[45]

Note: R is red (670 nm), G is green (540 nm), B is blue (480 nm), and NIR is near-infrared (803 nm).

We further leveraged the multiband option of our hyperspectral data (274 bands) and calculated thousands of combinations of a normalized difference index to identify new and possible band combinations suitable for  $\psi_{\text{leaf}}$  other than the already established 12 spectral indices used in this study. The normalized difference spectral index (NDSI) approach uses a two-band combination of reflectance [57]:

$$\text{NDSI} \text{ (unitless)} = \frac{b1 - b2}{b1 + b2} \quad (1)$$

where b1 and b2 are the reflectance values of any two wavelength bands. Such a normalization mitigates the influence of varying illumination conditions, isolating the relative difference between the selected bands [57].

Since each hyperspectral image contains 274 bands from 400 to 1000 nm, a total of 37,401 NDSI options could be derived from combining each pair of bands (i.e.,  $274 \times 273$  options divided by 2 to avoid duplications with inverted order) per image per individual. Each NDSI value was used in a simple linear regression against the  $\psi_{\text{leaf}}$ . After this, we selected the top-performing indices yielding the highest coefficient of determination ( $R^2$ ). First, we excluded indices that showed a high correlation for any two bands close to each other within a 10 nm interval. Then, we chose the index with the best correlation and added four more local maxima indices for all species datasets (Supplementary Figure S1). This process was conducted at the individual tree level, with spectral data analyzed separately for each tree.

A multivariable linear regression (MLR) model was tested with the top five indices, starting with simple regression and adding one index at a time to verify the effect of increasing the number of unique bands on the linear regression model's accuracy.

Finally, we averaged the spectral and  $\psi_{\text{leaf}}$  values for each plot (comprising five species) for each sampling date. We calculated a new NDSI using these plot-level averages and performed linear regressions between the spectral and the  $\psi_{\text{leaf}}$  data. This averaging aimed to develop models at the plot scale ('general' model). However, due to the reduction in sample size (fivefold fewer samples), machine learning models could not be applied to this dataset.

### 3.2. Machine Learning Algorithms

Only the five selected NDSIs exhibiting the highest correlation with  $\psi_{\text{leaf}}$  were used in three machine learning algorithms: random forest (RF), extreme gradient boosting (XGB), and support vector machine (SVM). We did not include the known spectral indices to avoid model overfitting because some of the known indices had overlapping bands and similar formulations as the NDSIs.

RF is an ensemble learning method that constructs multiple decision trees and aggregates their predictions, accounting for variations and reducing overfitting [58]. XGB is a scalable tree-boosting system that builds an ensemble of weak prediction models sequentially, with each successive model aiming to correct the errors of its predecessor [59]. SVM is a supervised learning algorithm that constructs hyperplanes in high-dimensional space to maximize the margin between classes. It can handle linear and nonlinear relationships through kernel functions, unlike RF and XGB, which are ensemble methods, thus requiring a larger sample size than SVM, which can learn from small samples [60,61]. The key parameters driving each ML algorithm are listed in Supplementary Table S1.

All models were trained on 70% of the data (training set) using fine-tuned hyperparameter (Supplementary Table S1) and cross-validation. The hyperparameter optimization for each model was performed using the scikit-learn randomgridsearchCV module. This module allows for the iterative search for the best combination of the algorithm-specific parameter(s), selecting the best estimators based on the highest-ranking performance of the models fitted. Finally, model performance was evaluated on the remaining unseen 30% (test dataset) using metrics such as the coefficient of determination ( $R^2$ ), the root mean squared error (RMSE), the ratio of performance to deviation (RPD), and the mean absolute error (MAE). An ensemble model (AVG) was also constructed by averaging the predictions from all individual models. Feature importance analysis was conducted to identify each model's most influential spectral indices.

In a subsequent step, species information was incorporated as a categorical variable using one-hot encoding and added to the input features [62]. The modeling process was repeated, including hyperparameter tuning and performance evaluation on the test set. The RMSE and  $R^2$  were calculated separately for each species to assess model performance across species.

The performance of the three machine learning algorithms (RF, XGBoost, and SVM) was compared with the performance of the linear spectral-based models. In addition, the machine learning algorithms were compared with each other, and their robustness was assessed using the residual prediction deviation (RPD [63,64]). RPD is defined as the ratio of the standard deviation of the actual measured  $\psi_{\text{leaf}}$  to the RMSE. We adopted the criteria of Mouazen et al. [65] for classifying RPD scores as follows: an RPD below 1.5 indicates that the model is not usable, an RPD between 1.5 and 2.0 indicates a possibility to distinguish between high- and low-value groups, and an RPD between 2.0 and 2.5 makes approximate quantitative predictions possible. The models were classified as good and excellent for RPD between 2.5 and 3.0 or above 3.0, respectively. Figure 4 presents the conceptual modeling framework and schemes.

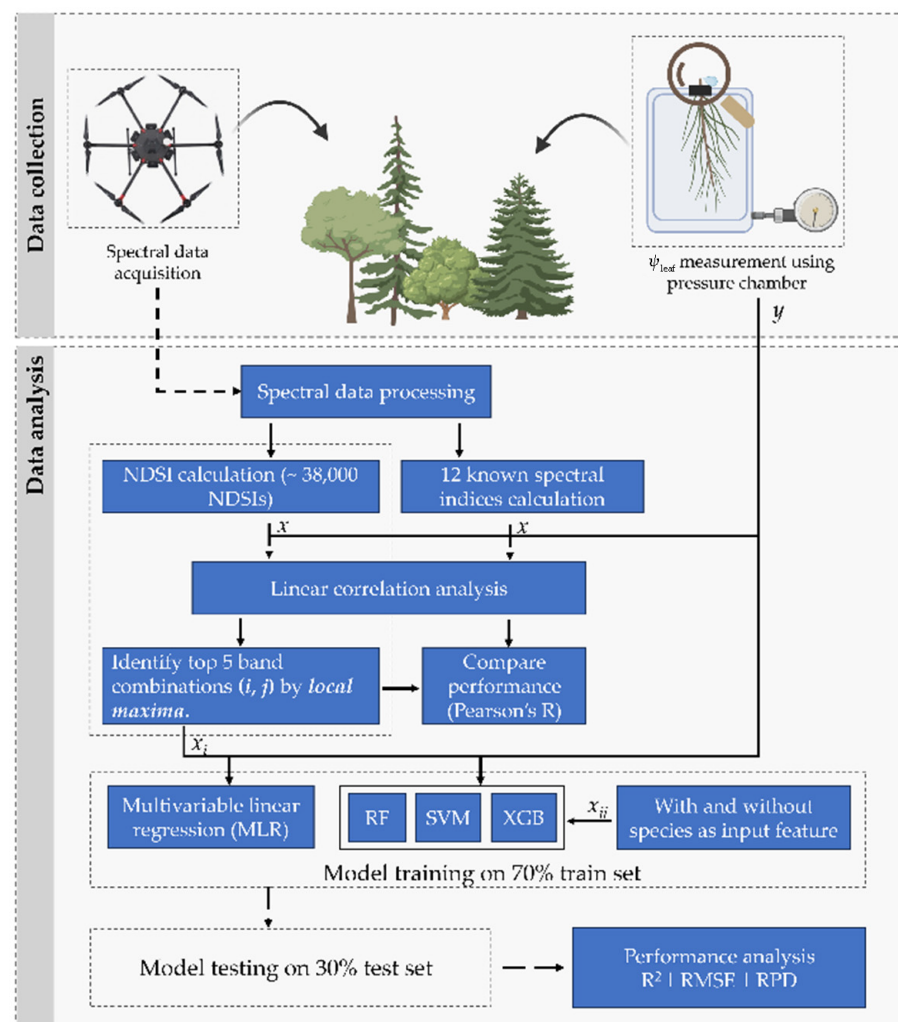


**Figure 4.** Schematics of the research framework, from the data collection to the machine learning modeling.  $x$  and  $y$  in the graph mean predictor and predicted variables, respectively.  $x_i$  and  $x_{ii}$  are the predictors using the top 5 NDSI without and with species as input features, respectively. RF, SVM, and XGB stand for random forest, support vector machine, and extreme gradient boosting algorithms.

### 3.3. Statistical Analysis

The ground-truth  $\psi_{leaf}$  measurements were tested for normality at  $p > 0.05$  sample with the Shapiro–Wilk test using the JMP 17 Pro statistical software (SAS Institute). All tests for statistical significance of model performance were performed within the Python pipeline at  $p < 0.05$ .

## 4. Results

### 4.1. Leaf Water Potential Dynamics and Correlation with Spectral Indices

We observed that  $\psi_{leaf}$  in the five species fluctuated between  $-1$  MPa and  $-5$  MPa and differed in magnitude as well as in their dynamics along the year (Figure 5). For example, Pine (*Pinus halepensis*) had overall the lowest  $\psi_{leaf}$ , with an average value of  $-2.56$  MPa over the year. Pine was also the species with the lowest inter-annual variance in  $\psi_{leaf}$ , along with the Carob (*Ceratonia siliqua*). In contrast, Cypress (*Cupressus sempervirens*) and Pistacia (*Pistacia sempervirens*) had both the largest  $\psi_{leaf}$  variance over the year, reaching during the dry months a  $\psi_{leaf}$  as low as  $-4.5$  MPa.

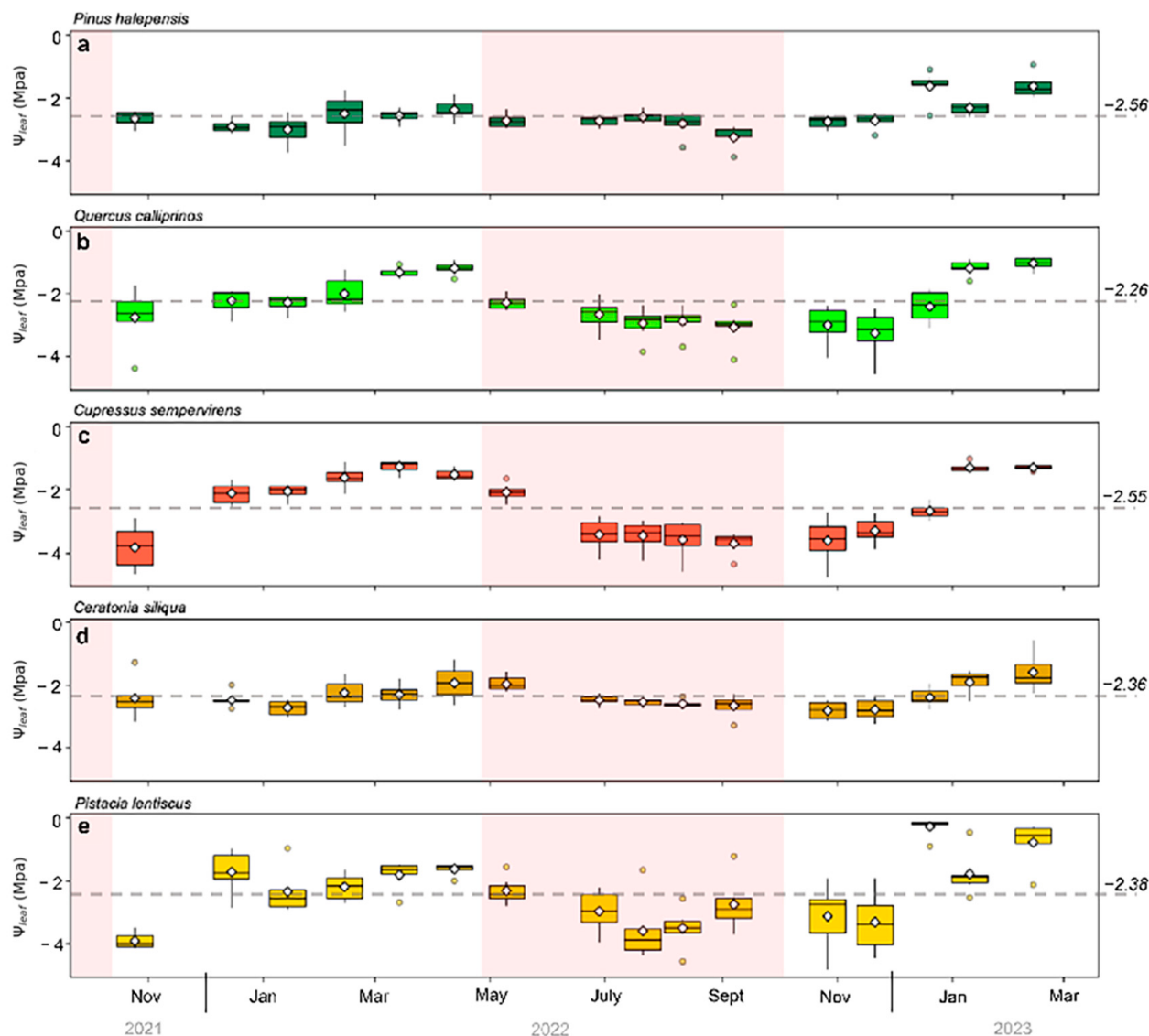


**Figure 5.** Seasonal variation in  $\psi_{leaf}$  throughout the study period across the five key woody species: (a) Pine, (b) Oak, (c) Cypress, (d) Carob, and (e) Pistacia. Each boxplot represents the interquartile range (IQR), with the horizontal line within each box indicating the median and the white diamond symbol the mean. Whiskers extend to the lowest and highest  $\psi_{leaf}$  within 1.5 times the IQR, and outliers are displayed as individual points. The horizontal gray dashed line represents the mean value throughout the study period, with its value in MPa next to the line. The pink shaded strips represent dry periods within the year.

Of the twelve known spectral indices, the best linear relationship was achieved with NDVI for Cypress (Pearson's  $R = 0.86$ ), while the other indices displayed only moderate-to-weak correlations with  $\psi_{leaf}$ . Pearson's correlations show that some indices had positive and some had negative linear relationships with  $\psi_{leaf}$  (Table 2). The correlations did not improve when the best NDSI was used against  $\psi_{leaf}$  (with bands 750 nm and 680 nm; Table 2). When considering all species, the linear models with the spectral indices had poor performance, with the best index being the NDVI, together with the best NDSI, both showing a Pearson's  $R$  of 0.57.

**Table 2.** Pearson's correlation coefficient ( $r$ ) between  $\psi_{leaf}$  and spectral indices, including the NDSI, per species, and for all species (All). Highlighted in bold are the highest  $R^2$  scores per index and the second-highest  $R^2$  scores in italics.

Index	Pine	Oak	Cypress	Carob	Pistacia	All
NDVI	<b>0.56</b>	<b>0.70</b>	<b>0.86</b>	<b>0.53</b>	0.54	<b>0.57</b>
PRI	0.31	-0.18	0.19	-0.18	0.55	0.09
940/960	0.20	0.24	0.31	0.29	0.48	0.29
940/960/NDVI	-0.51	-0.65	-0.84	-0.38	-0.34	-0.48
EVI2	0.23	0.10	-0.08	-0.06	0.24	0.08
COSBNDI	-0.32	-0.13	-0.39	-0.18	-0.63	-0.29
FOSBNDI	0.41	0.38	0.63	0.21	0.50	0.43
SAPSBNDI	0.11	0.14	0.49	0.26	0.60	0.27
WASCOSBNDI	-0.22	-0.16	0.26	0.03	0.13	0.03
NDWSI	0.15	0.21	0.50	0.27	0.60	0.29
NDWI	-0.52	-0.65	-0.83	-0.51	<b>-0.67</b>	-0.48
WI	-0.21	-0.27	-0.48	-0.26	-0.60	-0.31
NDSI (680/750)	0.55	0.69	<b>0.86</b>	<b>0.54</b>	0.60	<b>0.57</b>

The MLR model performed slightly better than the spectral indices, with  $R^2 = 0.40$  (compared to 0.32 for the NDVI and the best NDSI). It required nine bands and five pairs to produce the best linear regression model (Table 3).

**Table 3.** The multivariable linear regression (MLR) model performance for the highest-scoring NDSI combinations. Asterisks (\*) represent significant correlations at  $p < 0.001$ . Highlighted in bold are the best scores (highest  $R^2$  and lowest RMSE).

NDSI (Band1/Band2) Combinations	R2	RMSE
680/750	0.33 *	0.73
680/750, 530/623	0.35 *	0.72
680/750, 530/623, 660/940	0.35 *	0.72
680/750, 530/623, 660/940, 519/750	0.35 *	0.72
680/750, 530/623, 660/940, 519/750, 605/709	<b>0.40</b> *	<b>0.70</b>

#### 4.2. Machine Learning Models

The nonlinear ML models (RF, SVM, and XGB) were not better than MLR, but the performance improved when species was included as a feature (Table 4). The best model using species as a feature was SVM, with an  $R^2$  of 0.53 and an RPD of 1.47.

**Table 4.** Machine learning model performance for each algorithm and the averaged model using the three algorithms without and with species as a feature in the model. NDSI combinations of 680/750, 530/623, 605/709, 519/750, and 660/940 were used as input. All models were significant at  $p < 0.001$ . In bold are the best statistical scores (highest  $R^2$  and RPD, and lowest MAE, RMSE).

Model	Without Species				With Species			
	<i>R</i> <sup>2</sup>	MAE	RMSE	RPD	<i>R</i> <sup>2</sup>	MAE	RMSE	RPD
RF	0.40	0.59	0.74	1.30	0.42	0.59	0.74	1.32
SVM	0.35	0.58	0.77	1.25	<b>0.53</b>	<b>0.50</b>	<b>0.67</b>	<b>1.47</b>
XGB	0.40	0.58	0.74	1.30	0.47	0.57	0.71	1.38
Averaged model	<b>0.41</b>	<b>0.58</b>	<b>0.74</b>	<b>1.31</b>	0.52	0.52	0.67	1.46

All four models (MLR and the three ML algorithms) performed the best with similar NDSI band combinations. However, the importance of each NDSI combination was not the same, depending on whether the model included species (Figure 6) or did not include species as a feature (Figure 7).

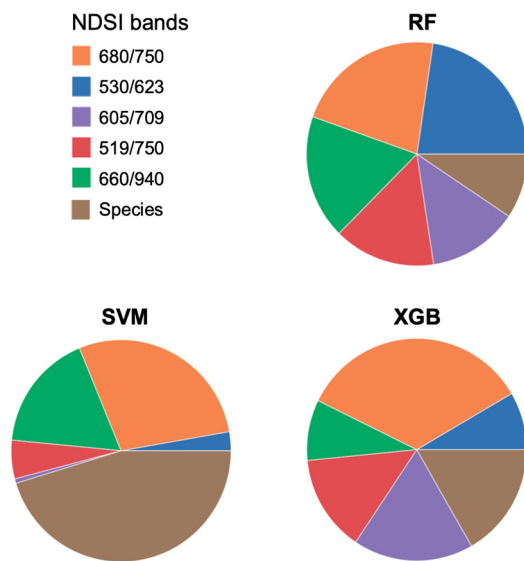


**Figure 6.** Feature importance of the NDSI pair bands in the different ML models when species was included as a feature.

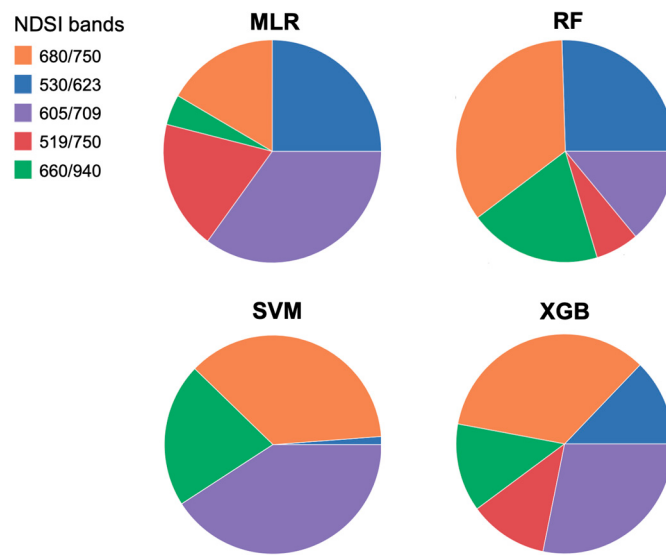


**Figure 7.** Feature importance of the NDSI pair bands in the MLR model and the different ML models when species were not included in the models.

Finally, the best ML model (SVM with species as a feature) predicted better  $\psi_{leaf}$  for Cypress and Pistacia than for the other species and had, specifically, low  $R^2$  for Pine and Carob (Figure 8).

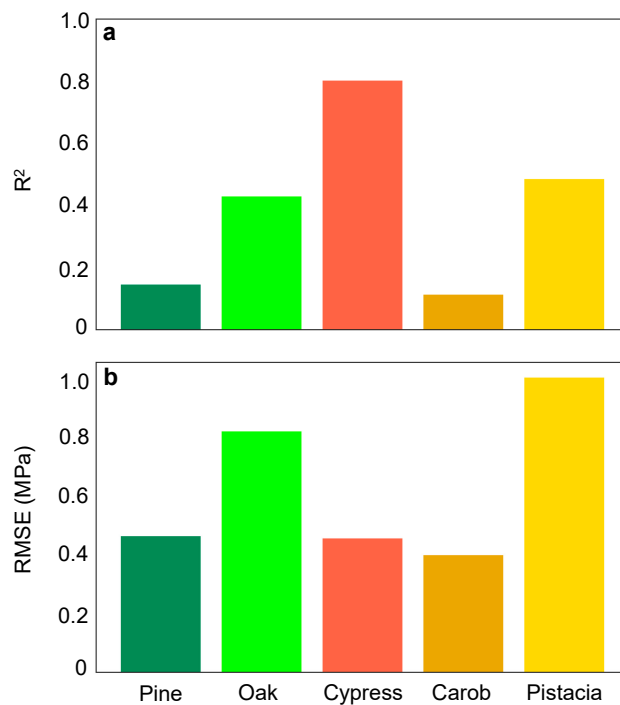


**Figure 8.** Performance of SVM model per species: (a)  $R^2$  of the correlation, (b) RMSE in MPa.

Table 5 summarizes the first and second-best models for each species. It is noticeable that a simple model based on a spectral index (mostly NDVI and NDSI) could predict  $\psi_{leaf}$  and that ML models did not significantly surpass the performance of the simple single-basis linear model while requiring much more spectral information. In addition, only Cypress reached a relatively high  $R^2$  in such models.

**Table 5.** A summary of the best and the second-best models for predicting  $\psi_{leaf}$  per species and for all species together (All). ML models are highlighted in gray, and spectral index models in green (light green for NDSI and dark green for vegetation index).

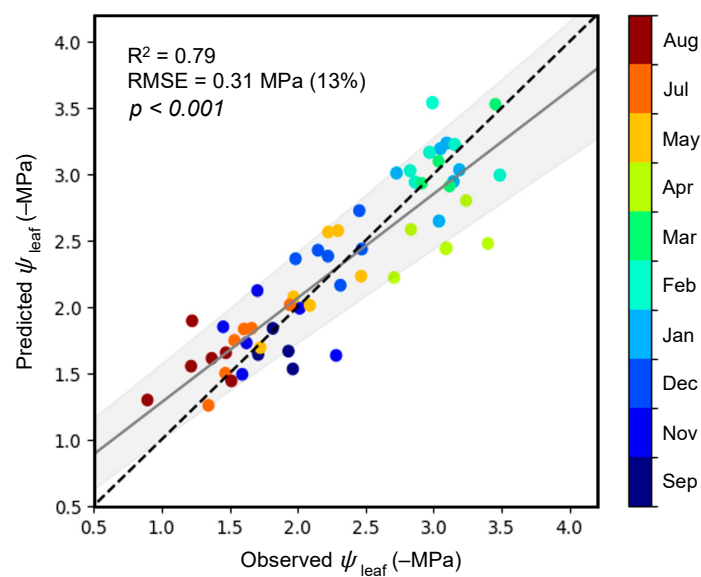
	Pine	Oak	Cypress	Carob	Pistacia	All
Best model	NDVI	NDVI NDSI	SVW (w/species)	NDSI	SVW (w/species)	SVW (w/species)
$R^2$	0.31	0.48	0.80	0.29	0.49	0.53
2nd best model	NDSI	MNDVI 940/960/NDVI	NDVI NDSI	NDVI	NDSI	Avg ML (w/o species)
$R^2$	0.30	0.42	0.74	0.28	0.44	0.41
Difference	0.01	0.06	0.06	0.01	0.05	0.12

■ ML model; ■ Spectral index.

#### 4.3. Averaging Data at the Plot Scale

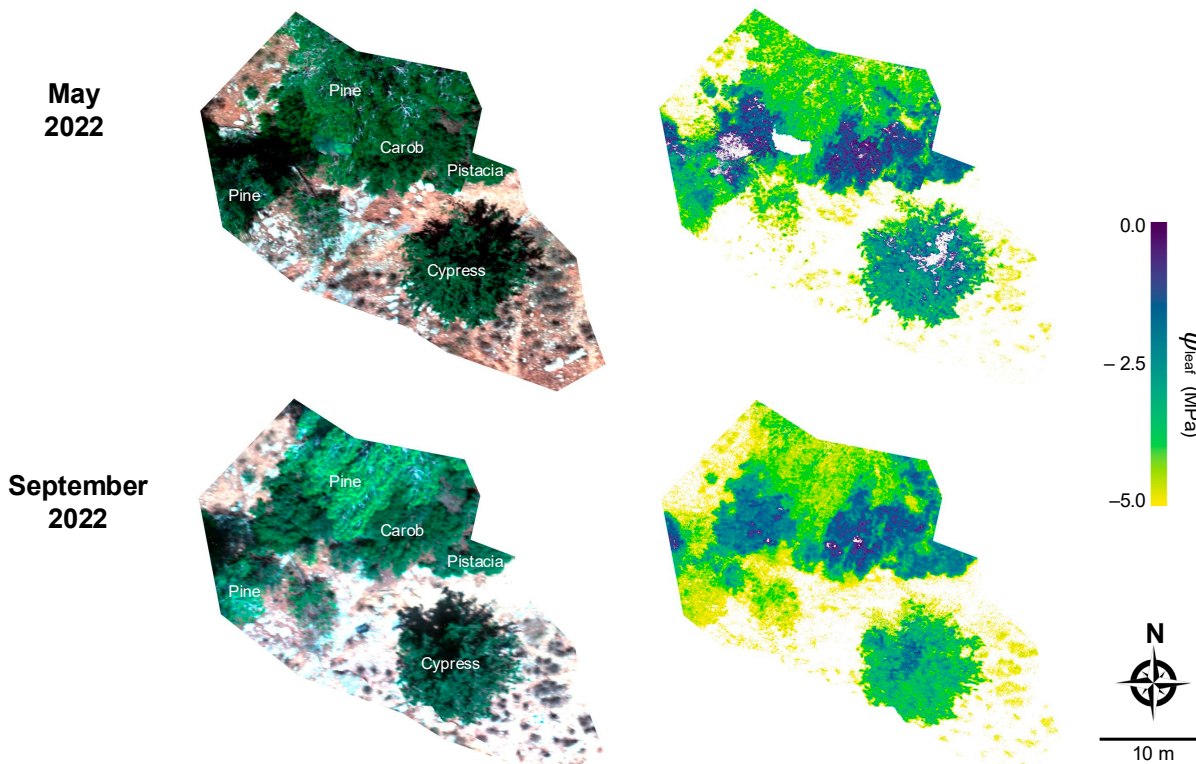
Due to the relatively moderate performance of the above species-specific models, we tested a ‘general’ model by averaging measurements over the entire plot (i.e., including all five species together). We found that NDSI with a band combination of 816 and 712 nm was the best predictor for  $\psi_{leaf}$  at the plot scale (Supplementary Figure S2).

Figure 9 shows observed versus predicted  $\psi_{leaf}$  using this ‘general’ model. The  $R^2$  of the correlation was 0.79, with a relative RMSE of 13%, significant at  $p < 0.001$ .



**Figure 9.** Predicted vs. observed  $\psi_{leaf}$  for plot-aggregated data. Each dot represents the mean value for all the species in a plot on a single date. Colors mark the months of the observed/predicted value. The broken line represents a 1:1 line.

Figure 10, showing the modeled  $\psi_{leaf}$  using the ‘general’ model, highlights the differences in  $\psi_{leaf}$  among the species (Pine with the lowest  $\psi_{leaf}$ , most negative values, Cypress with moderately negative  $\psi_{leaf}$ , and Carob with the least negative  $\psi_{leaf}$  values) and between the seasons (more negative values in September, at the end of the dry season, than in May, at the end of the rainy season).



**Figure 10.** The  $\psi_{leaf}$  map generated using the ‘general’ model and drone images acquired on two dates, one at the end of the dry season (September) and another at the end of the wet season (May).

## 5. Discussion

This study explored the use of hyperspectral imaging and machine learning models to estimate leaf water potential ( $\psi_{leaf}$ ) in a mixed Mediterranean forest at a high spatial resolution using drone imagery. We specifically hypothesized that  $\psi_{leaf}$  would be easier to model from the spectral data for species with a broader range of  $\psi_{leaf}$  values. This proved true since most models were much better for Cypress and Pistacia, which showed a more comprehensive range of  $\psi_{leaf}$  values along the season than the other species. We also hypothesized that machine learning algorithms should significantly enhance the ability to predict  $\psi_{leaf}$  compared to simple linear regression models using spectral indices, specifically the nonlinear models that account for more complex relationships. Indeed, our findings show that the SVM model was slightly superior to the simpler regression models using the spectral indices (Tables 2 and 4). However, except for Cypress and Pistacia, SVM was not better than simple spectral indices in predicting  $\psi_{leaf}$  (Table 5). Overall, simple linear regression with commonly used vegetation indices, like the NDVI, performed well enough to make the complex and data-demanding SVM model superfluous. Yet, the general performance of SVM above RF and XGB may be related to its ability to learn effectively with small sample datasets, thus taking advantage of the sensitivity of its support vectors to all sample data points, including outliers [61]. Also, SVM can map the dataset into high dimensional input space, where it looks for core differences between classes using the optimal hyperplane, which might have given it an added advantage when species were added as part of the feature, leading to an increased  $R^2$  of 0.35 to 0.53 (Table 4).

The observed variations in  $\psi_{leaf}$  among the five species (Figure 5) align with previous findings by Peñuelas et al. [32], reporting distinct water management characteristics in mixed Mediterranean forest species. This variability underscores the complexity of modeling water status in heterogeneous forest ecosystems. Pine exhibited the lowest average  $\psi_{leaf}$  ( $-2.56$  MPa) and the least inter-annual variance. In contrast, Cypress and Pistacia demonstrated the most considerable  $\psi_{leaf}$  variance, reaching as low as  $-4.5$  MPa during dry months. It is not surprising, then, that the model performance was much better for these two species. These species-specific differences in water potential dynamics highlight the importance of considering individual species' physiological responses when developing forest water status assessment models or at least considering stand density and species as factors.

As stated, most spectral indices showed a low correlation with  $\psi_{leaf}$  (Table 2), with the NDVI being the best predictor, particularly for Cypress ( $R^2 = 0.74$ ). The other spectral indices tested in this study exhibited suboptimal performance despite their established correlation with plant water status in previous studies. This discrepancy may be attributed to the predominant focus of these indices on leaf water content rather than  $\psi_{leaf}$  [22,44,50,56]. While the leaf water content directly influences spectral reflectance,  $\psi_{leaf}$  is a physiological parameter that reflects plant functionality and can vary in response to various factors, including water stress and changes in the ambient radiation environment. Elsayed et al. [55] demonstrated the distinction between these parameters by developing indices specifically for estimating  $\psi_{leaf}$ , independent of the leaf water content. However, the disparity between their experimental design (controlled climate chamber, handheld spectrometer, crop plants) and ours (forest canopies, hyperspectral camera at 60 m height) may explain the limited applicability of their indices in our study. Our results suggest that these indices may not translate directly to forest stands under natural conditions, where factors such as canopy structure, background soil reflectance, and atmospheric effects can influence spectral measurements.

Though using different bands, our findings align more closely with those of Stimson et al. [24], who studied two conifer species (*Pinus edulis* and *Juniperus monosperma*) in a forest

setting. They found that indices incorporating 980 nm and 1200 nm wavelength bands were significantly correlated with measured  $\psi_{leaf}$ , but the relationships differed between the two species. This species-specific variability is consistent with our observations, where Cypress and Pistacia showed stronger correlations with spectral indices than Pine and Carob. The high variability in  $\psi_{leaf}$  between species is also consistent with recent findings by Italiano et al. [25], who reported significant differences in hydraulic traits among Mediterranean forest species.

The evaluation of machine learning models, including RF, XGB, and SVM, resulted in the SVM being the best model, particularly when incorporating species as a feature (Table 4). While Sadiq et al. [30] and Virnodkar et al. [31] focused on other vegetation characteristics rather than  $\psi_{leaf}$  specifically, their work demonstrates the broader potential of machine learning in remote sensing applications for forest assessment. In our study, the performance varied across species, with Cypress and Pistacia showing better predictability compared to Pine, Oak, and Carob (Figure 8). This variation may be attributed to the higher inter-annual variance of  $\psi_{leaf}$  in Cypress and Pistacia, enabling stronger correlations between changes in leaf water potential and spectral indices. The improved performance of models incorporating species information highlights the importance of considering species-specific traits in mixed forest ecosystems. However, the practical application of such models in mixed forests remains challenging due to the difficulty in differentiating species in the image, especially when considering the most practical remote sensing use of satellites, which usually have a coarser spatial resolution. However, efforts seem successful in satellite and drone-based spectral differentiation of vegetation classes and types (e.g., [66,67]).

Our ‘general’ model, averaging all species at the plot scale, has a greater potential for satellite remote sensing use. This is because it indicates that species differentiation is not required. This ‘general’ model is based on two bands, one within the red-edge range (712 nm), which marks the inflection point from strong absorption by leaf chlorophyll in the visible region to structurally dominated reflectance in the NIR, which was the second band (816 nm) [68]. This is not surprising since band centering within the red-edge region is very sensitive to the slightest changes in chlorophyll content due to stress or LAI changes, resulting in either a blue shift—toward shorter wavelengths or a red shift—toward longer wavelengths [69–71]. The red and blue bands readily saturate at relatively low chlorophyll content or show an almost insignificant response to even small biochemical changes. Thus, the red-edge band is more likely to respond to changes in pigmentation and leaf cell or canopy structure. In contrast, bands within the visible regions are less sensitive to structure [72,73].

The plot-scale approach may offer a more robust method for assessing forest water status over larger areas, potentially bridging the gap between individual leaf measurements and landscape-scale assessments using satellite imagery. The improved performance at the plot scale has important implications for forest management and ecological monitoring. It suggests that while individual tree-level predictions may be challenging due to high variability, aggregating data at a broader scale can provide reliable estimates of forest water status. This approach could be convenient for assessing drought stress across forest stands or informing management decisions in planted forests, which comprise about half of the forested areas in Israel [35].

While promising, this ‘general’ model has two main limitations. First, it was generated at the plot scale, and the scalability to a finer scale, as shown in Figure 10, still needs to be verified. Nevertheless, the seasonal differences with more negative  $\psi_{leaf}$  observed at the end of the dry season than at the end of the wet season indicate that the model can reasonably capture temporal variations in forest water status. This temporal sensitivity is crucial for monitoring the impacts of seasonal drought and climate change on forest ecosystems, as

highlighted by Allen et al. [1] and reported by IPCC [2], even though the magnitude might be inaccurate. Moreover, the clear differentiation between species in the modeled  $\psi_{leaf}$ , in accordance with the measured values, further strengthens our confidence in the model's ability to distinguish between species-specific water management strategies. The second limitation concerns the generality of the model. In other words, how reliable can this model be when transferred to another area? Since plots were relatively homogeneous in their species distribution, the model might need to be adjusted with, at least, a factor considering the stand density (when using satellite imagery) or/and by considering different species mixing at the pixel level. However, considering that the species in our study area are common Mediterranean species and the climate is a typical Mediterranean one, our model may be applied to similar regions elsewhere. Nevertheless, further testing should be conducted in different environments to ensure the model's general applicability.

Finally,  $\psi_{leaf}$  is not a trivial parameter to detect directly and remotely. Without the invention of the pressure chamber and applying very high pressure (>50 bar in this study), it would have been very difficult to predict otherwise. Non-destructive  $\psi_{leaf}$  determination in the field by a few methods is still being tested. Thus, though challenging, our remote sensing effort to predict  $\psi_{leaf}$  proved successful and can be further used to detect  $\psi_{leaf}$  changes across mixed forest stands. Future research should include drought-stressed plots, which are the target of a future stress alert method.

## 6. Summary and Conclusions

Analysis applying vegetation indices and various ML models to the entire dataset without incorporating species information resulted in weak to moderate correlations. The absence of a significant advantage for more complex ML models can be explained by the intrinsic variability in leaf spectral features across different species within the forest. When species information was included as a feature, the correlation improved for SVM but was still weak to be superior to the simple spectral index model.

A 'general' plot scale model without species-specific differentiation performed much better. This finding is promising since the model can be used with satellite images to derive  $\psi_{leaf}$  at a coarser yet continuous spatial resolution. The fact that a 'general' model was better than all species-specific models highlights the inherent challenges of applying accurate remote sensing techniques in mixed-species forests, where interspecies variability is significant. These results suggest that plot-level aggregation may offer a more robust approach for assessing forest water status over larger areas. Still, such a conclusion must be further tested since the plots in our study area were relatively homogeneous regarding species distribution and density. In cases where fine-scale evaluation is required, and species classification is available, our findings indicate that the SVM model can be relatively effective in addressing these challenges.

Our approach facilitates the precise monitoring of  $\psi_{leaf}$ , which can inform targeted forest conservation efforts, adaptive management strategies, and interventions tailored to species-specific drought vulnerabilities, thereby enhancing ecosystem resilience in the face of increasing drought stress.

**Supplementary Materials:** The following supporting information can be downloaded at: <https://www.mdpi.com/article/10.3390/rs17010106/s1>; Supplementary Table S1. Optimized hyperparameters for Random Forest (RF), Support Vector Ma-chine (SVM), and XGBoost (XGB); Supplementary Figure S1. Correlation maps of all possible two-band combinations with normalized difference vegetation index (NDSI) and the measured  $\psi_{leaf}$  ( $N = 246$ ); Supplementary Figure S2. Correlation maps of all possible two-band combinations with normalized difference vegetation index (NDSI) and the measured  $\psi_{leaf}$  averaged over the entire plot ( $N = 56$ ).

**Author Contributions:** Conceptualization, D.H. and T.K.; Methodology, N.F., A.Y., S.O., L.R., Y.M., T.K. and D.H.; Software, N.F., Y.Y., G.M., Y.M. and D.H.; Validation, N.F., Y.Y., T.K. and D.H.; Formal analysis, N.F. and D.H.; Investigation, N.F., S.O., T.K. and D.H.; Resources, T.K. and D.H.; Data curation, N.F., A.Y., S.O., L.R., G.M. and T.K.; Writing—original draft, N.F. and D.H.; Writing—review & editing, N.F., Y.Y., G.M., T.K. and D.H.; Supervision, D.H.; Project administration, D.H. and T.K.; Funding acquisition, D.H. and T.K. All authors have read and agreed to the published version of the manuscript.

**Funding:** This research was funded by the Jewish National Fund (KKL) via KKL chief scientist grant #2145 (430/21). N.F., Y.Y., and G.M. were partly funded by this grant.

**Data Availability Statement:** The original contributions presented in this study are included in the article. Further inquiries can be directed to the corresponding author.

**Acknowledgments:** We thank Gil Lerner for flying the drone and assisting with fieldwork and Itzik Ben-Shabbat from IDO for assisting with the drone and flight permits. We also thank the Jewish National Fund (KKL) for supporting this study via KKL chief scientist grant #2145 (430/21). N.F. is an M.Sc. student at the Faculty of Agriculture, Food, and Environment under the supervision of D.H.

**Conflicts of Interest:** The authors declare no conflict of interest.

## References

- Allen, C.D.; Macalady, A.K.; Chenchouni, H.; Bachelet, D.; McDowell, N.; Vennetier, M.; Kitzberger, T.; Rigling, A.; Breshears, D.D.; Hogg, E.H.; et al. A global overview of drought and heat-induced tree mortality reveals emerging climate change risks for forests. *For. Ecol. Manag.* **2010**, *259*, 660–684. [[CrossRef](#)]
- IPCC. *Climate Change 2023: Synthesis Report. Contribution of Working Groups I, II and III to the Sixth Assessment Report of the Intergovernmental Panel on Climate Change*; Core Writing Team, Lee, H., Romero, J., Eds.; IPCC: Geneva, Switzerland, 2023.
- Klein, T.; Cahanovitc, R.; Sprintsin, M.; Herr, N.; Schiller, G. A nation-wide analysis of tree mortality under climate change: Forest loss and its causes in Israel 1948–2017. *For. Ecol. Manag.* **2019**, *432*, 840–849. [[CrossRef](#)]
- Patsiou, T.S.; Shestakova, T.A.; Klein, T.; di Matteo, G.; Sbay, H.; Chambel, M.R.; Zas, R.; Voltas, J. Intraspecific responses to climate reveal nonintuitive warming impacts on a widespread thermophilic conifer. *New Phytol.* **2020**, *228*, 525–540. [[CrossRef](#)]
- Hartmann, H.; Moura, C.F.; Anderegg, W.R.L.; Ruehr, N.K.; Salmon, Y.; Allen, C.D.; Arndt, S.K.; Breshears, D.D.; Davi, H.; Galbraith, D.; et al. Research frontiers for improving our understanding of drought-induced tree and forest mortality. *New Phytol.* **2018**, *218*, 15–28. [[CrossRef](#)] [[PubMed](#)]
- Jarvis, P.G. The Interpretation of the Variations in Leaf Water Potential and Stomatal Conductance Found in Canopies in the Field. *Philos. Trans. R. Soc. Lond. B. Biol. Sci.* **1976**, *273*, 593–610.
- Sack, L.; Ball, M.; Brodersen, C.; Davis, S.; Des Marais, D.; Donovan, L.; Givnish, T.; Hacke, U.; Huxman, T.; Jansen, S.; et al. Plant hydraulics as a central hub integrating plant and ecosystem function: Meeting report for “Emerging Frontiers in Plant Hydraulics” (Washington, DC, May 2015). *Plant. Cell Environ.* **2016**, *39*, 2085–2094. [[CrossRef](#)] [[PubMed](#)]
- Scholander, P.F.; Hammel, H.T.; Bradstreet, E.D.; Hemmingsen, E.A. Sap pressure in vascular plants. *Science* **1965**, *148*, 339–346. [[CrossRef](#)] [[PubMed](#)]
- Kerr, J.T.; Ostrovsky, M. From space to species: Ecological applications for remote sensing. *Trends Ecol. Evol.* **2003**, *18*, 299–305. [[CrossRef](#)]
- Konings, A.G.; Rao, K.; Steele-Dunne, S.C. Macro to micro: Microwave remote sensing of plant water content for physiology and ecology. *New Phytol.* **2019**, *223*, 1166–1172. [[CrossRef](#)]
- Asner, G.P.; Martin, R.E.; Anderson, C.B.; Kryston, K.; Vaughn, N.; Knapp, D.E.; Bentley, L.P.; Shenkin, A.; Salinas, N.; Sinca, F.; et al. Scale dependence of canopy trait distributions along a tropical forest elevation gradient. *New Phytol.* **2017**, *214*, 973–988. [[CrossRef](#)]
- Zarco-Tejada, P.J.; Rueda, C.A.; Ustin, S.L. Water content estimation in vegetation with MODIS reflectance data and model inversion methods. *Remote Sens. Environ.* **2003**, *85*, 109–124. [[CrossRef](#)]
- Ullah, S.; Skidmore, A.K.; Naeem, M.; Schlerf, M. An accurate retrieval of leaf water content from mid to thermal infrared spectra using continuous wavelet analysis. *Sci. Total Environ.* **2012**, *437*, 145–152. [[CrossRef](#)]
- Helman, D.; Yungstein, Y.; Mulero, G.; Michael, Y. High-Throughput Remote Sensing of Vertical Green Living Walls (VGWs) in Workplaces. *Remote Sens.* **2022**, *14*, 3485. [[CrossRef](#)]
- Konings, A.G.; Gentine, P. Global variations in ecosystem-scale isohydricity. *Glob. Change Biol.* **2017**, *23*, 891–905. [[CrossRef](#)] [[PubMed](#)]

16. Anderson, L.O.; Malhi, Y.; Aragão, L.E.O.C.; Ladle, R.; Arai, E.; Barbier, N.; Phillips, O. Remote sensing detection of droughts in Amazonian forest canopies. *New Phytol.* **2010**, *187*, 733–750. [CrossRef] [PubMed]
17. Ceccato, P.; Flasse, S.; Tarantola, S.; Jacquemoud, S.; Grégoire, J.-M. Detecting vegetation leaf water content using reflectance in the optical domain. *Remote Sens. Environ.* **2001**, *77*, 22–33. [CrossRef]
18. Coops, N.C.; Stone, C.; Culvenor, D.S.; Chisholm, L.A.; Merton, R.N. Chlorophyll content in eucalypt vegetation at the leaf and canopy scales as derived from high resolution spectral data. *Tree Physiol.* **2003**, *23*, 23–31. [CrossRef] [PubMed]
19. Helman, D.; Mussery, A. Using Landsat satellites to assess the impact of check dams built across erosive gullies on vegetation rehabilitation. *Sci. Total Environ.* **2020**, *730*, 138873. [CrossRef] [PubMed]
20. Roberts, D.A.; Barbara, S.; Roth, K.; Perroy, R.L. *Spectral and Spatial Methods of Hyperspectral Image Analysis for Estimation of Biophysical and Biochemical Properties of Agricultural Crops*; CRC Press: Boca Raton, FL, USA, 2011; ISBN 6087858334. [CrossRef]
21. Thenkabail, P.S.; Lyon, J.G.; Huete, A. (Eds.) *Hyperspectral Indices and Image Classifications for Agriculture and Vegetation*, 2nd ed.; CRC Press: Boca Raton, FL, USA, 2018. [CrossRef]
22. Raj, R.; Walker, J.P.; Vinod, V.; Pingale, R.; Naik, B.; Jagarlapudi, A. Leaf water content estimation using top-of-canopy airborne hyperspectral data. *Int. J. Appl. Earth Obs. Geoinf.* **2021**, *102*, 102393. [CrossRef]
23. Peñuelas, J.; Fillla, I.; Serrano, L.; Savé, R. Cell wall elasticity and Water Index (R970 nm/R900 nm) in wheat under different nitrogen availabilities. *Int. J. Remote Sens.* **1996**, *17*, 373–382. [CrossRef]
24. Stimson, H.C.; Breshears, D.D.; Ustin, S.L.; Kefauver, S.C. Spectral sensing of foliar water conditions in two co-occurring conifer species: *Pinus edulis* and *Juniperus monosperma*. *Remote Sens. Environ.* **2005**, *96*, 108–118. [CrossRef]
25. Italiano, S.S.P.; Julio Camarero, J.; Borghetti, M.; Colangelo, M.; Pizarro, M.; Ripullone, F. Radial growth, wood anatomical traits and remote sensing indexes reflect different impacts of drought on Mediterranean forests. *For. Ecol. Manag.* **2023**, *548*, 121406. [CrossRef]
26. Othman, Y.; Steele, C.; VanLeeuwen, D.; Heerema, R.; Bawazir, S.; St. Hilaire, R. Remote sensing used to detect moisture status of pecan orchards grown in a desert environment. *Int. J. Remote Sens.* **2014**, *35*, 949–966. [CrossRef]
27. Wang, Z.; Sun, Z.; Lu, S. Optimal vegetation index for assessing leaf water potential using reflectance factors from the adaxial and abaxial surfaces. *Comput. Electron. Agric.* **2020**, *172*, 105337. [CrossRef]
28. Li, J.; Wijewardane, N.K.; Ge, Y.; Shi, Y. Improved chlorophyll and water content estimations at leaf level with a hybrid radiative transfer and machine learning model. *Comput. Electron. Agric.* **2023**, *206*, 107669. [CrossRef]
29. Li, W.; Pacheco-Labrador, J.; Migliavacca, M.; Miralles, D.; Hoek van Dijke, A.; Reichstein, M.; Forkel, M.; Zhang, W.; Frankenberg, C.; Panwar, A.; et al. Widespread and complex drought effects on vegetation physiology inferred from space. *Nat. Commun.* **2023**, *14*, 4640. [CrossRef] [PubMed]
30. Sadiq, M.A.; Sarkar, S.K.; Raisa, S.S. Meteorological drought assessment in northern Bangladesh: A machine learning-based approach considering remote sensing indices. *Ecol. Indic.* **2023**, *157*, 111233. [CrossRef]
31. Virnodkar, S.S.; Pachghare, V.K.; Patil, V.C.; Jha, S.K. Remote sensing and machine learning for crop water stress determination in various crops: A critical review. *Precis. Agric.* **2020**, *21*, 1121–1155. [CrossRef]
32. Peñuelas, J.; Sardans, J.; Filella, I.; Estiarte, M.; Llusia, J.; Ogaya, R.; Carnicer, J.; Bartrons, M.; Rivas-Ubach, A.; Grau, O.; et al. Impacts of Global Change on Mediterranean Forests and Their Services. *Forests* **2017**, *8*, 463. [CrossRef]
33. Rog, I.; Tague, C.; Jakoby, G.; Megidish, S.; Yaakobi, A.; Wagner, Y.; Klein, T. Interspecific Soil Water Partitioning as a Driver of Increased Productivity in a Diverse Mixed Mediterranean Forest. *J. Geophys. Res. Biogeosci.* **2021**, *126*, e2021JG006382. [CrossRef]
34. Lapidot, O.; Ignat, T.; Rud, R.; Rog, I.; Alchanatis, V.; Klein, T. Use of thermal imaging to detect evaporative cooling in coniferous and broadleaved tree species of the Mediterranean maquis. *Agric. For. Meteorol.* **2019**, *271*, 285–294. [CrossRef]
35. Amir, S.; Rechtman, O. The development of forest policy in Israel in the 20th century: Implications for the future. *For. Policy Econ.* **2006**, *8*, 35–51. [CrossRef]
36. Fassnacht, F.E.; Latifi, H.; Stereńczak, K.; Modzelewska, A.; Lefsky, M.; Waser, L.T.; Straub, C.; Ghosh, A. Review of studies on tree species classification from remotely sensed data. *Remote Sens. Environ.* **2016**, *186*, 64–87. [CrossRef]
37. Pozner, E.; Bar-On, P.; Livne-Luzon, S.; Moran, U.; Tsamir-Rimon, M.; Dener, E.; Schwartz, E.; Rotenberg, E.; Tatarinov, F.; Preisler, Y.; et al. A hidden mechanism of forest loss under climate change: The role of drought in eliminating forest regeneration at the edge of its distribution. *For. Ecol. Manag.* **2022**, *506*, 119966. [CrossRef]
38. Rog, I.; Hilman, B.; Fox, H.; Yalin, D.; Qubaja, R.; Klein, T. Increased belowground tree carbon allocation in a mature mixed forest in a dry versus a wet year. *Glob. Change Biol.* **2024**, *30*, e17172. [CrossRef]
39. Israel Meteorological Service. Available online: <http://www.ims.gov.il> (accessed on 29 December 2024).
40. Sternberg, M.; Golodets, C.; Gutman, M.; Perevolotsky, A.; Kigel, J.; Henkin, Z. No precipitation legacy effects on above-ground net primary production and species diversity in grazed Mediterranean grassland: A 21-year experiment. *J. Veg. Sci.* **2017**, *28*, 260–269. [CrossRef]
41. Boyer, J.S. Leaf Water Potentials Measured with a Pressure Chamber. *Plant Physiol.* **1967**, *42*, 133–137. [CrossRef] [PubMed]

42. Ritchie, G.A.; Hinckley, T.M. The Pressure Chamber as an Instrument for Ecological Research. *Adv. Ecol. Res.* **1975**, *9*, 165–254. [[CrossRef](#)]
43. Savitzky, A.; Golay, M.J.E. Smoothing and Differentiation of Data by Simplified Least Squares Procedures. *Anal. Chem.* **1964**, *36*, 1627–1639. [[CrossRef](#)]
44. Azar, M.; Mulero, G.; Oppenheimer-Shaanan, Y.; Helman, D.; Klein, T. Aboveground responses to belowground root damage detected by non-destructive sensing metrics in three tree species. *Forestry* **2023**, *96*, 672–689. [[CrossRef](#)]
45. Peñuelas, J.; Filella, I.; Biel, C.; Serrano, L.; Savé, R. The reflectance at the 950–970 nm region as an indicator of plant water status. *Int. J. Remote Sens.* **1993**, *14*, 1887–1905. [[CrossRef](#)]
46. Sadeh, R.; Avneri, A.; Tubul, Y.; Lati, R.N.; Bonfil, D.J.; Peleg, Z.; Herrmann, I. Chickpea leaf water potential estimation from ground and VENµS satellite. *Precis. Agric.* **2024**, *25*, 1–26. [[CrossRef](#)]
47. Helman, D.; Osem, Y.; Yakir, D.; Lensky, I.M. Relationships between climate, topography, water use and productivity in two key Mediterranean forest types with different water-use strategies. *Agric. For. Meteorol.* **2017**, *232*, 319–330. [[CrossRef](#)]
48. Helman, D.; Bahat, I.; Netzer, Y.; Ben-Gal, A.; Alchanatis, V.; Peeters, A.; Cohen, Y. Using Time Series of High-Resolution Planet Satellite Images to Monitor Grapevine Stem Water Potential in Commercial Vineyards. *Remote Sens.* **2018**, *10*, 1615. [[CrossRef](#)]
49. Mulero, G.; Jiang, D.; Bonfil, D.J.; Helman, D. Use of thermal imaging and the photochemical reflectance index (PRI) to detect wheat response to elevated CO<sub>2</sub> and drought. *Plant. Cell Environ.* **2023**, *46*, 76–92. [[CrossRef](#)] [[PubMed](#)]
50. Hunt, E.R., Jr.; Daughtry, C.; Qu, J.; Wang, L.; Hao, X. Comparison of hyperspectral retrievals with vegetation water indices for leaf and canopy water content. *Proc. SPIE Int. Soc. Opt. Eng.* **2011**, *8156*, 5. [[CrossRef](#)]
51. Gao, B. NDWI—A normalized difference water index for remote sensing of vegetation liquid water from space. *Remote Sens. Environ.* **1996**, *58*, 257–266. [[CrossRef](#)]
52. McFeeters, S.K. The use of the Normalized Difference Water Index (NDWI) in the delineation of open water features. *Int. J. Remote Sens.* **1996**, *17*, 1425–1432. [[CrossRef](#)]
53. Kriegler, F.J.; Malila, W.A.; Nalepka, R.F.; Richardson, W. Preprocessing Transformations and Their Effects on Multispectral Recognition. In Proceedings of the Sixth International Symposium on Remote Sensing of Environment; Arbor, A., Ed.; University of Michigan: Michigan, MI, USA, 1969; pp. 97–131.
54. Gamon, J.A.; Peñuelas, J.; Field, C.B. A narrow-waveband spectral index that tracks diurnal changes in photosynthetic efficiency. *Remote Sens. Environ.* **1992**, *41*, 35–44. [[CrossRef](#)]
55. Elsayed, S.; Mistele, B.; Schmidhalter, U. Can changes in leaf water potential be assessed spectrally? *Funct. Plant Biol.* **2011**, *38*, 523–533. [[CrossRef](#)]
56. Jiang, Z.; Huete, A.R.; Didan, K.; Miura, T. Development of a two-band enhanced vegetation index without a blue band. *Remote Sens. Environ.* **2008**, *112*, 3833–3845. [[CrossRef](#)]
57. Inoue, Y.; Peñuelas, J.; Miyata, A.; Mano, M. Normalized difference spectral indices for estimating photosynthetic efficiency and capacity at a canopy scale derived from hyperspectral and CO<sub>2</sub> flux measurements in rice. *Remote Sens. Environ.* **2008**, *112*, 156–172. [[CrossRef](#)]
58. Breiman, L. Random Forests. *Mach. Learn.* **2001**, *45*, 5–32. [[CrossRef](#)]
59. Chen, T.; Guestrin, C. XGBoost: A scalable tree boosting system. In Proceedings of the 22nd ACM SIGKDD International Conference on Knowledge Discovery and Data Mining, San Francisco, CA, USA, 13–17 August 2016; Association for Computing Machinery: New York, NY, USA, 2016; Volume 13, pp. 785–794.
60. Cortes, C.; Vapnik, V. Support-vector networks. *Mach. Learn.* **1995**, *20*, 273–297. [[CrossRef](#)]
61. Kok, Z.H.; Mohamed Shariff, A.R.; Alfatni, M.S.M.; Khairunniza-Bejo, S. Support Vector Machine in Precision Agriculture: A review. *Comput. Electron. Agric.* **2021**, *191*, 106546. [[CrossRef](#)]
62. Pinhanez, C.S.; Cavalin, P.R. Exploring the Advantages of Dense-Vector to One-Hot Encoding of Intent Classes in Out-of-Scope Detection Tasks. *arXiv* **2022**, arXiv:2205.09021.
63. Agussabti; Rahmaddiansyah; Satriyo, P.; Munawar, A.A. Data analysis on near infrared spectroscopy as a part of technology adoption for cocoa farmer in Aceh Province, Indonesia. *Data Br.* **2020**, *29*, 105251. [[CrossRef](#)]
64. Sahoo, M.M.; Perach, O.; Shachter, A.; Gonda, I.; Porwal, A.; Dudai, N.; Herrmann, I. Spectral estimation of carnosic acid content in *in vivo* rosemary plants. *Ind. Crops Prod.* **2022**, *187*, 115292. [[CrossRef](#)]
65. Mouazen, A.M.; De Baerdemaeker, J.; Ramon, H. Effect of wavelength range on the measurement accuracy of some selected soil constituents using visual-near infrared spectroscopy. *J. Near Infrared Spectrosc.* **2006**, *14*, 189–199. [[CrossRef](#)]
66. Weil, G.; Lensky, I.M.; Resheff, Y.S.; Levin, N. Using Near-Surface Observations for Optimizing the Timing of Overhead Image Acquisition for Applied Mapping of Woody Vegetation Species. In Proceedings of the IGARSS 2018–2018 IEEE International Geoscience and Remote Sensing Symposium, Valencia, Spain, 22–27 July 2018; pp. 5398–5401.
67. Weil, G.; Lensky, I.M.; Levin, N. Using ground observations of a digital camera in the VIS-NIR range for quantifying the phenology of Mediterranean woody species. *Int. J. Appl. Earth Obs. Geoinf.* **2017**, *62*, 88–101. [[CrossRef](#)]
68. Croft, H.; Chen, J.M. Leaf Pigment Content. *Compr. Remote Sens.* **2018**, *3*, 117–142. [[CrossRef](#)]

- 
69. Thenkabail, P.S.; Lyon, J.G.; Huete, A. Hyperspectral Remote Sensing of Vegetation. CRC Press: Boca Raton, FL, USA, 2016; ISBN 978-1-4398-4538-7.
  70. Xie, Q.; Dash, J.; Huang, W.; Peng, D.; Qin, Q.; Mortimer, H.; Casa, R.; Pignatti, S.; Laneve, G.; Pascucci, S.; et al. Vegetation Indices Combining the Red and Red-Edge Spectral Information for Leaf Area Index Retrieval. *IEEE J. Sel. Top. Appl. Earth Obs. Remote Sens.* **2018**, *11*, 1482–1492. [[CrossRef](#)]
  71. Guyot, G.; Baret, F.; Major, D.J. High spectral resolution: Determination of spectral shifts between the red and infrared. *Int. Arch. Photogramm. Remote Sens.* **1988**, *11*, 750–760. [[CrossRef](#)]
  72. Kumar, L.; Schmidt, K.; Dury, S.; Skidmore, A. *Imaging Spectrometry and Vegetation Science BT—Imaging Spectrometry: Basic Principles and Prospective Applications*; Meer, F.D., van der, J., De, S.M., Eds.; Springer: Dordrecht, The Netherlands, 2001; pp. 111–155, ISBN 978-0-306-47578-8.
  73. Dong, T.; Liu, J.; Shang, J.; Qian, B.; Ma, B.; Kovacs, J.M.; Walters, D.; Jiao, X.; Geng, X.; Shi, Y. Assessment of red-edge vegetation indices for crop leaf area index estimation. *Remote Sens. Environ.* **2019**, *222*, 133–143. [[CrossRef](#)]

**Disclaimer/Publisher’s Note:** The statements, opinions and data contained in all publications are solely those of the individual author(s) and contributor(s) and not of MDPI and/or the editor(s). MDPI and/or the editor(s) disclaim responsibility for any injury to people or property resulting from any ideas, methods, instructions or products referred to in the content.